International Journal of Bifurcation and Chaos, Vol. 27, No. 1 (2017) 1750010 (17 pages)

DOI: 10.1142/S0218127417500109

Bursting Types and Bifurcation Analysis in the Pre-Bötzinger Complex Respiratory Rhythm Neuron

Jing Wang*,†, Bo Lu*,‡, Shenquan Liu§ and Xiaofang Jiang¶
School of Mathematics,
South China University of Technology,
Guangzhou 510640, P. R. China
†*wangjing901225@gmail.com*
‡*cheersnow@163.com*
§*mashqliu@scut.edu.cn*
¶*jiangxf5@yeah.net*

Received May 7, 2016; Revised September 10, 2016

Many types of neurons and excitable cells could intrinsically generate bursting activity, even in an isolated case, which plays a vital role in neuronal signaling and synaptic plasticity. In this paper, we have mainly investigated bursting types and corresponding bifurcations in the pre-Bötzinger complex respiratory rhythm neuron by using fast–slow dynamical analysis. The numerical simulation results have showed that for some appropriate parameters, the neuron model could exhibit four distinct types of fast–slow bursters. We also explored the bifurcation mechanisms related to these four types of bursters through the analysis of phase plane. Moreover, the first Lyapunov coefficient of the Hopf bifurcation, which can decide whether it is supercritical or subcritical, was calculated with the aid of MAPLE software. In addition, we analyzed the codimension-two bifurcation for equilibria of the whole system and gave a detailed theoretical derivation of the Bogdanov–Takens bifurcation. Finally, we obtained expressions for a fold bifurcation curve, a nondegenerate Hopf bifurcation curve, and a saddle homoclinic bifurcation curve near the Bogdanov–Takens bifurcation point.

Keywords: Bursting; Bogdanov–Takens bifurcation; fast–slow dynamical analysis; potassium channel; external electric field; pre-Bötzinger complex.

1. Introduction

As a small region in the ventrolateral medulla, the pre-Bötzinger complex (pre-BötC) is considered to be the genesis of respiratory rhythm in mammals and can autonomously generate rhythmic activity without external input [Smith *et al.*, 1991; Smith *et al.*, 2013; Johnson *et al.*, 1994; Koshiya & Smith, 1999]. Recordings from the medulla *in vitro* show that this intrinsic rhythmic activity persists even after blockade of inhibitory synaptic connections [Feldman & Smith, 1989; Shao & Feldman, 1997]; in other words, this activity can be triggered by a single bursting pacemaker neuron located in the medullary pre-BötC [Butera *et al.*, 1999; Rekling & Feldman, 1998; Thoby-Brisson & Ramirez, 2001; Rybak *et al.*, 2004].

In this context, we study the pre-BötC neuron which was modeled in the Hodgkin–Huxley style proposed by Butera *et al.* [1999]. The single neuron model includes persistent sodium current, fast

*These authors contributed equally to this work and should be considered as co-first authors.
§Author for correspondence

sodium current, delayed rectifier potassium current and leakage current. Among these four kinds of current, the delayed rectifier potassium current is worthy of study owing to its important role in neuronal activities and transitions between spiking and bursting [Rybak *et al.*, 2003]. Bacak *et al.* [2016] recently investigated endogenous bursting properties by changing extracellular potassium concentration. They found that endogenous bursting activity is the result of a particular relationship between the delayed rectifier potassium current and leakage current. Shevtsova *et al.* [2003] focused on the conditions that could trigger or suppress endogenous population oscillations and the specific roles of voltage-gated potassium current in single pacemaker neurons. Negro *et al.* [2001] showed that a transition from bursting to tonic spiking could be elicited by elevating extracellular potassium concentration, whose effect is to attenuate the potassium current.

Bursting oscillation has been widely researched in neuronal models and certain excitable cells because of its significant roles in information processing and transmission [Izhikevich & Hippensteadt, 2004], and its functional effects in reliable communication among neurons [Izhikevich, 2003; Lisman, 1997; Eyherabide *et al.*, 2009] and neuronal synaptic plasticity [Wang, 1999; Huerta & Lisman, 1995]. As a unit of neural information and the primary discharge pattern, bursting involves two processes: one is the relatively fast process associated with generation of action potentials, and another is relatively slow process that modulates fast variables [Izhikevich, 2000, 2005]. So far, some important methods were proposed to reveal the bifurcation mechanism of transitions between the quiescent state and the spiking state. The singular perturbation theory has made great progress since the turn of the last century [Smith, 1985; Hoppensteadt, 1993; Mishchenko *et al.*, 1994; Fenichel, 1979; Jones, 1995]. In addition, the approach of fast–slow dynamics analysis has been extensively applied to topologically classify several typical bursting types [Izhikevich, 2000; Yang & Lu, 2007; Wang *et al.*, 2008; Wang *et al.*, 2015; Lu *et al.*, 2016]. Based on one-parameter and two-parameter bifurcation analysis, the generation and transition of bursting types could be explained clearly.

The main purpose of the present study is to explore bursting oscillations and related bifurcations in the pre-BötC neuron model. Four types of fast–slow bursters are found as the maximum conductance of delayed rectifier potassium current (g_{K}) is varied. And the mechanisms of generating bursting are investigated in detail using fast–slow dynamics analysis and phase plane analysis. For one-parameter bifurcation analysis, we compute the first Lyapunov coefficient of the Hopf bifurcation to determine whether it is supercritical or subcritical. Furthermore, we give the two-parameter bifurcation analysis of the whole system in the (V_e, g_{K})-plane, and analyze the Bogdanov–Takens bifurcation. At the same time, we obtain a fold bifurcation curve, a Hopf bifurcation curve, and a homoclinic bifurcation curve near the Bogdanov–Takens bifurcation point.

The rest of this paper is arranged as follows. Section 2 describes the single pre-BötC neuron model and introduces the tools for computer simulations. In Sec. 3, we present detailed codimension-one bifurcation diagrams and phase portraits of the fast subsystem. We explore the properties of the Hopf bifurcation point in Sec. 4. Section 5 investigates the codimension-two bifurcation analysis of the whole system. Finally, we conclude in Sec. 6.

2. Model and Methods

Our research model is based on a single-compartment Hodgkin–Huxley formalism as described by Butera *et al.* [1999]. The model contains persistent sodium current, fast sodium current, delayed rectifier potassium current and leakage current. In this study, we think about the effect of external electric field. Once a cell is exposed to an external electric field, the induced trans-membrane potential emerges which superimposes on the primary ionic membrane potential [Polk & Postow, 1996; Kotnik *et al.*, 2011; Che *et al.*, 2012; Che *et al.*, 2014]; that is to say, the total membrane potential is substituted by $V + V_e$. Then the original current balance equation is modified as follows:

$$\begin{aligned} C\frac{d(V+V_e)}{dt} &= -g_{\mathrm{NaP}} m_{\mathrm{NaP}\infty}(V) h (V + V_e - E_{\mathrm{NaP}}) \\ &\quad - g_{\mathrm{Na}} m^3_{\mathrm{Na}\infty}(V)(1-n)(V + V_e - E_{\mathrm{Na}}) \\ &\quad - g_{\mathrm{K}} n^4 (V + V_e - E_{\mathrm{K}}) - g_{\mathrm{L}}(V + V_e - E_{\mathrm{L}}), \end{aligned} \tag{1}$$

where C is the whole cell membrane capacitance, V is the membrane potential, and V_e is the induced membrane potential reflecting the influence of the external electric field. The value of V_e is set to 0 mV unless otherwise noted. Since we only consider the influence of DC electric field, the term CdV_e/dt on the left of Eq. (1) is equal to 0.

The dynamics of gating variables n and h are described according to

$$\frac{dn}{dt} = \frac{\alpha_n(V)(1-n) - \beta_n(V)n}{\tau_n}, \tag{2}$$

$$\frac{dh}{dt} = \frac{\alpha_h(V)(1-h) - \beta_h(V)h}{\tau_h}. \tag{3}$$

The steady-state voltage-dependent (in)activation functions are given by

$$m_{\mathrm{NaP}\infty}(V) = \frac{1}{\left\{1 + \exp\left[-\dfrac{V+40}{6}\right]\right\}}, \tag{4}$$

$$m_{\mathrm{Na}\infty}(V) = \frac{1}{\left\{1 + \exp\left[-\dfrac{V+34}{5}\right]\right\}}, \tag{5}$$

$$\alpha_x(V) = \exp\left[-\frac{V-\theta_x}{2\sigma_x}\right], \quad x = n, h, \tag{6}$$

$$\beta_x(V) = \exp\left[\frac{V-\theta_x}{2\sigma_x}\right], \quad x = n, h. \tag{7}$$

Throughout the rest of this paper, except for g_{K} and V_e, all the other parameters involved in this model are fixed as given in Table 1. The model has been integrated by the fourth-order Runge–Kutta algorithm and the step size is 0.01 ms. The bifurcation diagrams and phase portraits are performed using MATCONT software [Dhooge *et al.*, 2003; Dhooge *et al.*, 2006].

Table 1. Parameter values for the pre-BötC neuron model.

Membrane Capacitance (pF)	$C = 21$
Time constants (ms)	$\tau_n = 20$, $\tau_h = 20\,000$
Conductance constants (nS)	$g_{\mathrm{NaP}} = 2.8$, $g_{\mathrm{Na}} = 28$, $g_{\mathrm{L}} = 2.8$
Reversal potentials (mV)	$E_{\mathrm{NaP}} = 50$, $E_{\mathrm{Na}} = 50$, $E_{\mathrm{K}} = -85$, $E_{\mathrm{L}} = -57.5$
Other kinetics parameters (mV)	$\theta_n = -29$, $\theta_h = -48$, $\sigma_n = -4$, $\sigma_h = 6$

3. Bursting Type Analysis

In the fast–slow dynamics analysis, since τ_h is several orders of magnitudes faster than C and τ_n, the variable h changes at a far slower pace than the other variables V and n for the same time scale. Hence, the whole system (1)–(3) can be decomposed into a fast subsystem (1) and (2), and a slow subsystem (3). And the slow variable h is treated as a bifurcation parameter. Then, the bifurcation curve for equilibria of the fast subsystem complies with the following equations:

$$\begin{aligned} &g_{\mathrm{NaP}} m_{\mathrm{NaP}\infty}(V)h(V - E_{\mathrm{NaP}}) \\ &\quad + g_{\mathrm{Na}} m^3_{\mathrm{Na}\infty}(V)(1-n)(V - E_{\mathrm{Na}}) \\ &\quad + g_{\mathrm{K}} n^4 (V - E_{\mathrm{K}}) + g_{\mathrm{L}}(V - E_{\mathrm{L}}) = 0, \end{aligned} \tag{8}$$

$$\alpha_n(V)(1-n) - \beta_n(V)n = 0. \tag{9}$$

The h-nullcline satisfies:

$$h = \frac{\alpha_h(V)}{\alpha_h(V) + \beta_h(V)}. \tag{10}$$

In this section, we shall show the numerical results from the bifurcation analysis of the fast subsystem (1)–(2). Through numerical calculations, we find that four completely different waveforms appear with the maximum conductance of delayed rectifier potassium current ranges $g_{\mathrm{K}} \in [3.82, 4.76)$ nS, $g_{\mathrm{K}} \in [4.76, 6.5)$ nS, $g_{\mathrm{K}} \in [6.5, 14.14)$ nS, and $g_{\mathrm{K}} \in [14.14, 25.8]$ nS. Within these ranges, the values of g_{K} are separately picked as 4.7 nS, 4.8 nS, 12 nS and 15 nS to show the characteristics of these four discharge patterns. Before presenting the numerical results, we explain the emerging symbols in the text below: LP_i $(i = 1, 2)$ represents the fold bifurcations of an equilibrium point; H represents the Hopf bifurcation of an equilibrium point; LPC_i $(i = 1, 2)$ represents the tangent bifurcations of limit cycles; HC represents the saddle homoclinic bifurcation. For the meaning of these bifurcations, the reader is referred to [Guckenheimer & Holmes, 1983; Kuznetsov, 1998]. In the codimension-one bifurcation diagrams, the symbols $V_{\max}$ and $V_{\min}$ separately denote the maximum value and the minimum value of the corresponding limit cycle. The dashed–dotted line represents the slow variable h-nullcline. The solid and dashed lines separately denote the stable and unstable equilibria (or limit cycles).

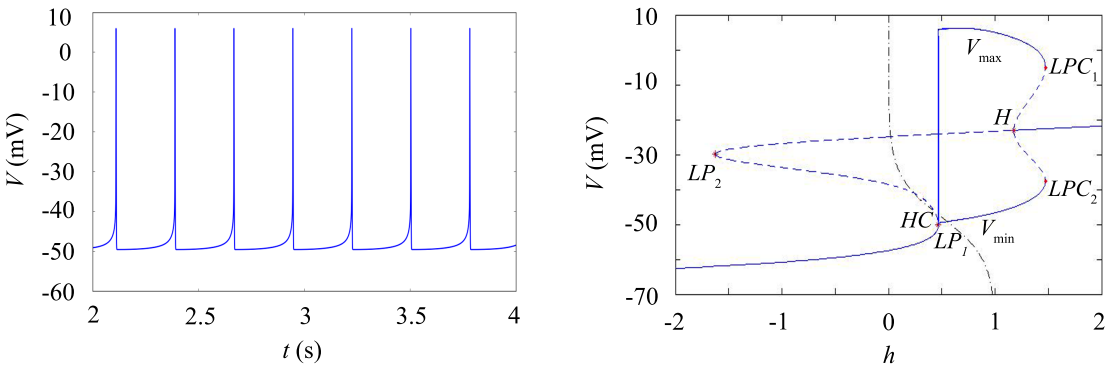

Fig. 1. The fast–slow dynamics of "circle/homoclinic" bursting via the "circle/homoclinic" hysteresis loop for $g_K = 15\,nS$. (a) Time evolution of the membrane potential and (b) fast–slow dynamics analysis of the fast subsystem. The dashed–dotted line represents the slow variable h-nullcline. The solid and dashed lines separately denote the stable and unstable equilibria (or limit cycles).

3.1. "*Circle/homoclinic*" *bursting via the* "*circle/homoclinic*" *hysteresis loop*

By using MATCONT software [Dhooge *et al.*, 2003; Dhooge *et al.*, 2006], the membrane potential and the bifurcation diagram for equilibria of the fast subsystem for $g_K = 15\,nS$ are shown in Figs. 1(a) and 1(b), respectively. From Fig. 1(b), we can see there is an S-shaped curve of steady state in the (h, V)-plane, where the solid line denotes stable equilibria and the dashed line denotes unstable ones. The S-shaped curve is made up of three branches. On the lower branch, the equilibria are all stable nodes. The middle branch is composed of unstable saddles. On the upper branch, the equilibrium is a stable focus or an unstable focus, whose stability changes via a Hopf bifurcation point H with $h = 1.177609$.

To analyze the generating process of spiking through bifurcations related to quiescence and discharge state, we append the spiking trajectory and the h-nullcline to Fig. 1(b). During the quiescent state, the neuron follows the lower branch of equilibria to the right. At the right fold bifurcation LP_1, the stable node and unstable saddle merge into one, and then disappear. Meanwhile, a stable limit cycle appears and goes through the point LP_1. Hence, the resting state switches to the repetitive spiking via the fold bifurcation on the invariant circle ($SNIC$). When V exceeds the h-nullcline, h begins to decrease. Until the spiking state reaches the point HC, which is a saddle on the middle branch with $h = 0.46778$. So a saddle homoclinic orbit forms and the repetitive spiking switches to the resting state. The same bifurcations form the hysteresis loop. According to the classification of fast–slow dynamics analysis [Izhikevich, 2000], this type of bursting pattern belongs to "circle/homoclinic" bursting via the "circle/homoclinic" hysteresis loop.

To understand the properties of this bursting type in detail, we apply the phase plane analysis to present the phase portraits on the (V, n)-plane with different values of h in Fig. 1(b). The filled dot, hollow dot and hollow pentagram in Figs. 2(a)–2(c) separately denote stable equilibrium, unstable equilibrium and fold bifurcation point. The red closed curve in Fig. 2(b) represents the stable limit cycle and the purple curve in Fig. 2(c) represents the saddle homoclinic orbit. Arrows indicate the direction of the vector field. It is shown in Fig. 2(a) that when $h = 0.46$, the fast subsystem has a stable node, a saddle and an unstable focus. With the increase of h, the stable node and the saddle are gradually approaching each other, and they coalesce at the fold bifurcation LP_1 and then disappear. At the same time, a stable limit cycle is generated from this fold bifurcation point. Thus, the resting state switches to repetitive spiking via fold bifurcation on the invariant circle. The hollow pentagram in Fig. 2(b) represents the bifurcation point $SNIC$. As h decreases to 0.46778, the closed orbit meets the saddle of the middle branch and forms a homoclinic orbit in Fig. 2(c), namely, a saddle homoclinic bifurcation takes place. Hence, the neuron transits from repetitive spiking to resting state via the homoclinic bifurcation.

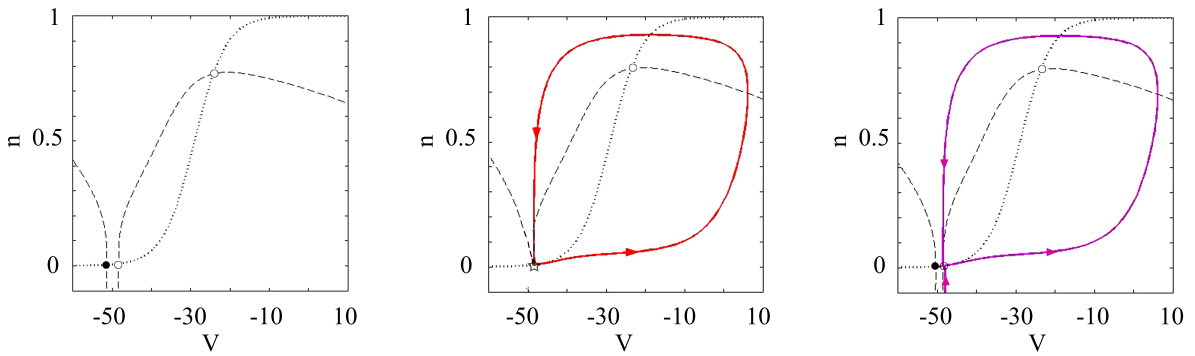

Fig. 2. Examples of phase portraits on the (V, n)-plane with different values of the slow variable h. (a) $h = 0.46$, (b) $h = 0.468326$ and (c) $h = 0.46778$. Here the dashed line and dotted line indicate V-nullcline and n-nullcline, respectively. The filled dot, hollow dot and hollow pentagram separately denote stable equilibrium, unstable equilibrium and fold bifurcation point. The red closed curve in phase portrait (b) represents the stable limit cycle and the purple curve in phase portrait (c) represents the homoclinic orbit. Arrows indicate directions of trajectories.

3.2. "*Fold/homoclinic*" *bursting via the* "*fold/homoclinic*" *hysteresis loop*

For the second type of bursting as we analyze next as shown in Fig. 3(a), the corresponding bifurcation diagram of the fast subsystem with respect to the slow variable h is shown in Fig. 3(b). There is also a S-shaped equilibria bifurcation curve in the (h, V)-plane. The separation of the lower and middle branches is fold bifurcation LP_1 with $h = 0.468326$; the separation of the upper and middle branches is another fold bifurcation LP_2 with $h = -1.661421$. This type of bursting is slightly different from the former case. At the right knee LP_1, the stable node and the saddle coalesce and annihilate each other. Besides, a stable limit cycle emerges and fails to pass through the point LP_1. Thereby, the resting state switches to the repetitive spiking via a fold bifurcation. Then h decreases and the spiking state reaches the saddle at HC on the middle branch with $h = 0.46035$, and a saddle homoclinic orbit forms. Hence, the repetitive spiking switches to the resting state via a saddle homoclinic bifurcation. The same bifurcations form the hysteresis loop. Depending on the classification of fast–slow dynamics analysis [Izhikevich, 2000], this type of bursting pattern belongs to "fold/homoclinic" bursting via the "fold/homoclinic" hysteresis loop (or "square-wave" bursting).

Similarly, we use the phase plane analysis to analyze properties of equilibria and periodic orbit on the (V, n)-plane with different values of h in

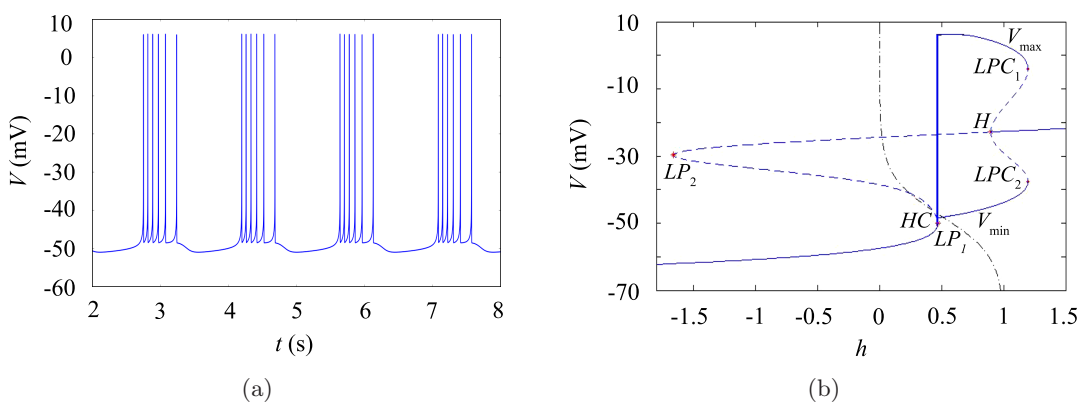

Fig. 3. The fast–slow dynamics of "fold/homoclinic" bursting via the "fold/homoclinic" hysteresis loop for $g_K = 12$ nS. (a) Time evolution of the membrane potential and (b) fast–slow dynamics analysis of the fast subsystem. The dashed–dotted line represents the slow variable h-nullcline. The solid and dashed lines separately denote the stable and unstable equilibria (or limit cycles).

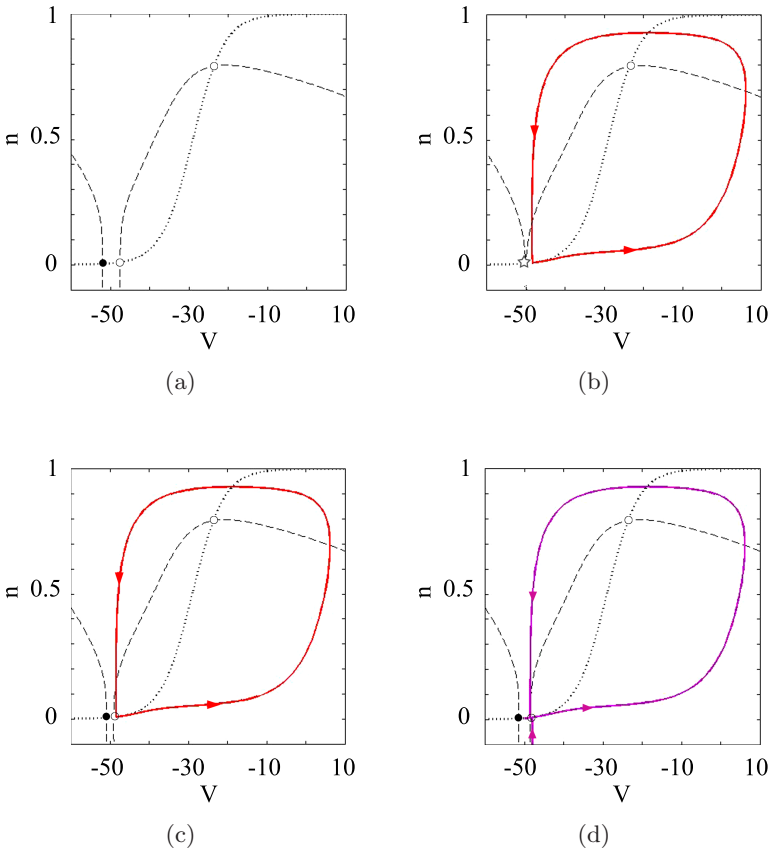

Fig. 4. Examples of phase portraits on the (V, n)-plane with different values of the slow variable h. (a) $h = 0.45$, (b) $h = 0.468326$, (c) $h = 0.465$ and (d) $h = 0.46035$. Here the dashed line and dotted line indicate V-nullcline and n-nullcline, respectively. The filled dot, hollow dot and hollow pentagram separately denote stable equilibrium, unstable equilibrium and fold bifurcation point. Red closed curves in phase portraits (b) and (c) represent the stable limit cycles and the purple curve in phase portrait (d) represents the homoclinic orbit. Arrows indicate directions of trajectories.

Fig. 3(b). It is shown in Fig. 4(a) that when $h = 0.45$, the fast subsystem has three equilibria, which are a stable node, a saddle and an unstable focus. When $h = 0.468326$, the stable node and the saddle merge into one so that a fold bifurcation occurs and a periodic orbit exists. Moreover, the fold bifurcation is away from the generated limit cycle. With the decrease of h, the fast subsystem has three equilibria and a stable limit cycle as shown in Fig. 4(c). As h decreases to 0.46035, a saddle homoclinic orbit forms with a stable node and an unstable focus.

3.3. "*Fold circle/homoclinic*" *bursting via the "fold/homoclinic" hysteresis loop*

When $g_K = 4.8\,\text{nS}$, the neuron exhibits the third type of bursting as shown in Fig. 5(a). Figure 5(b) is the one-parameter bifurcation diagram of the fast subsystem. The analysis method of burster classification is similar to the previous two types of bursting. The quiescent state disappears via fold limit cycle bifurcation and the spiking state disappears via saddle homoclinic orbit bifurcation. The formation of the hysteresis loop is different. The bifurcation of the transitions from the down-state to the up-state is fold bifurcation LP_1, and the bifurcation of the transitions from the up-state to the down-state is saddle homoclinic orbit bifurcation HC. Thus, this bursting mode is defined as "fold circle/homoclinic" bursting via the "fold/homoclinic" hysteresis loop.

It is shown in Fig. 6(a) that when $h = 0.35$, the fast subsystem has three equilibria, which are a stable node, a saddle and an unstable focus. When $h = 0.468326$, the stable node and the saddle merge into one so that a fold bifurcation occurs and no periodic orbit exists. With the decrease of h, the fast subsystem has three equilibria again. As h decreases to 0.4554251, an unstable limit cycle appears in Fig. 6(d). With the further decrease of h, a stable and an unstable limit cycle coexist with a

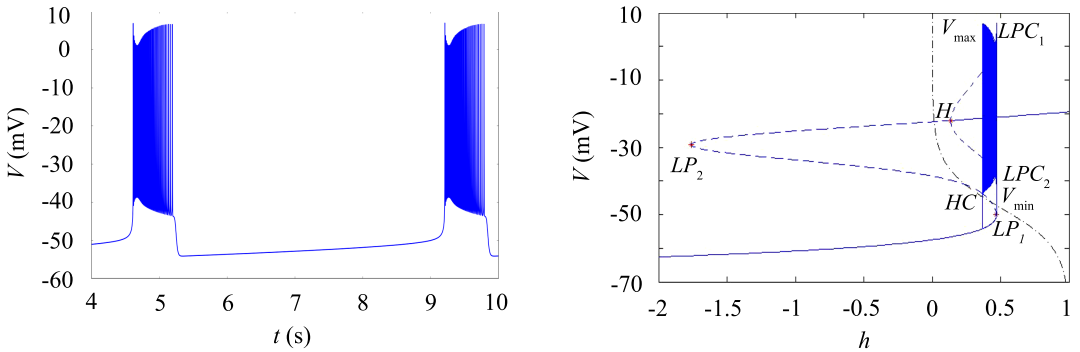

(a) (b)

Fig. 5. The fast–slow dynamics of "fold circle/homoclinic" bursting via the "fold/homoclinic" hysteresis loop for $g_K = 4.8$ nS. (a) Time evolution of the membrane potential and (b) fast–slow dynamics analysis of the fast subsystem. The dashed–dotted line represents the slow variable h-nullcline. The solid and dashed lines separately denote the stable and unstable equilibria (or limit cycles).

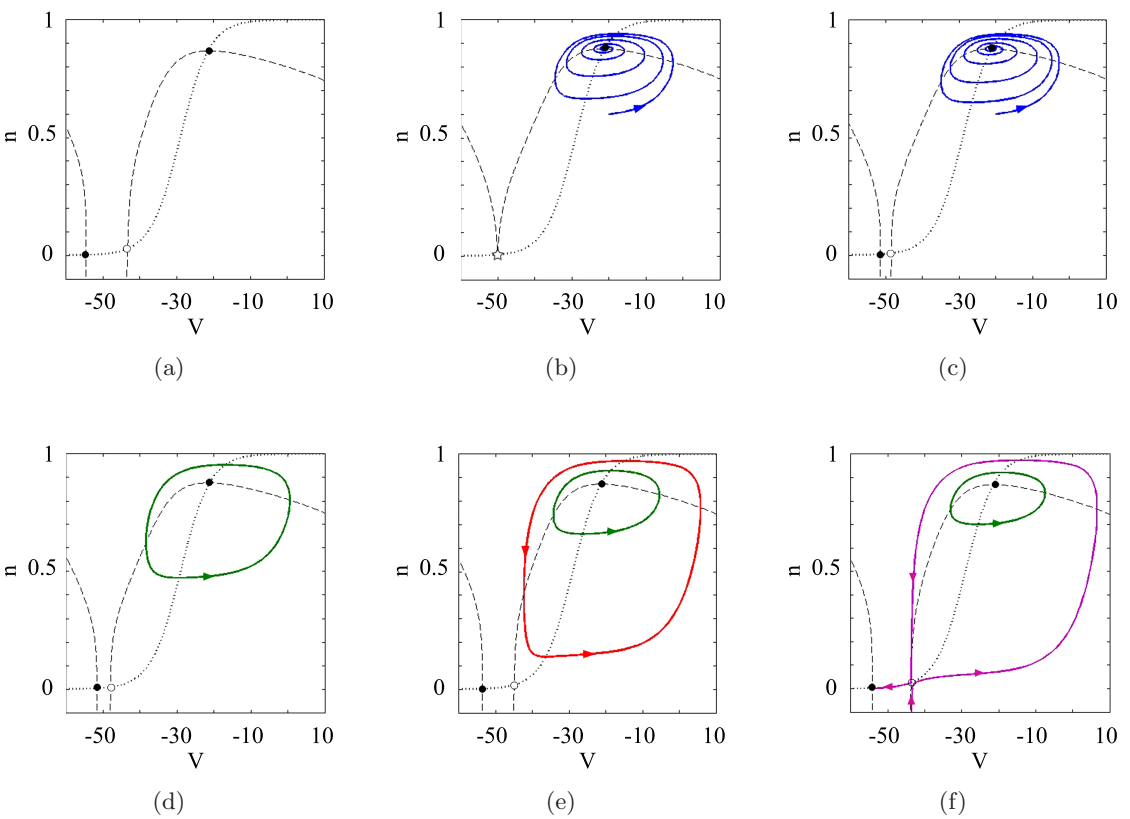

(a) (b) (c) (d) (e) (f)

Fig. 6. Examples of phase portraits on the (V, n)-plane with different values of the slow variable h. (a) $h = 0.35$, (b) $h = 0.468326$, (c) $h = 0.46$, (d) $h = 0.4554251$, (e) $h = 0.4$ and (f) $h = 0.36625$. Here the dashed line and dotted line indicate V-nullcline and n-nullcline, respectively. The filled dot, hollow dot and hollow pentagram separately denote stable equilibrium, unstable equilibrium and fold bifurcation point. The red closed curve in phase portrait (e) represents the stable limit cycle; green closed curves in phase portraits (d)–(f) represent the unstable limit cycles; the purple curve in phase portrait (f) represents the homoclinic orbit. Arrows indicate directions of trajectories.

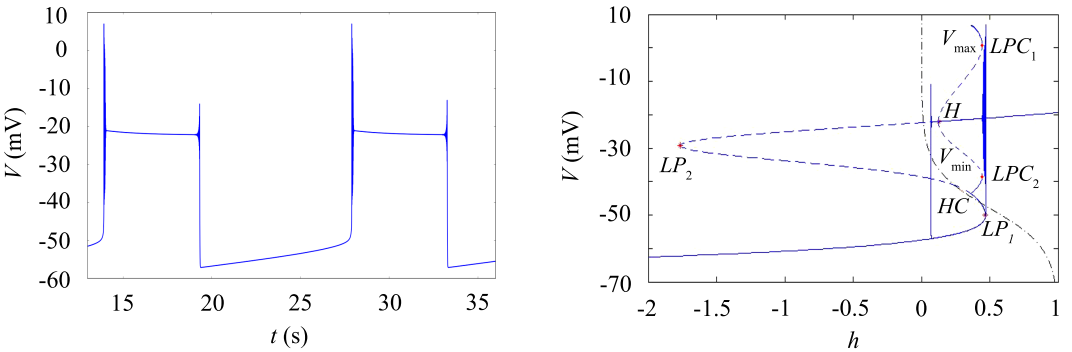

(a) (b)

Fig. 7. The fast–slow dynamics of "fold/Hopf" hysteresis loop bursting of point–point type for $g_K = 4.7$ nS. (a) Time evolution of the membrane potential and (b) fast–slow dynamics analysis of the fast subsystem. The dashed–dotted line represents the slow variable h-nullcline. The solid and dashed lines separately denote the stable and unstable equilibria (or limit cycles).

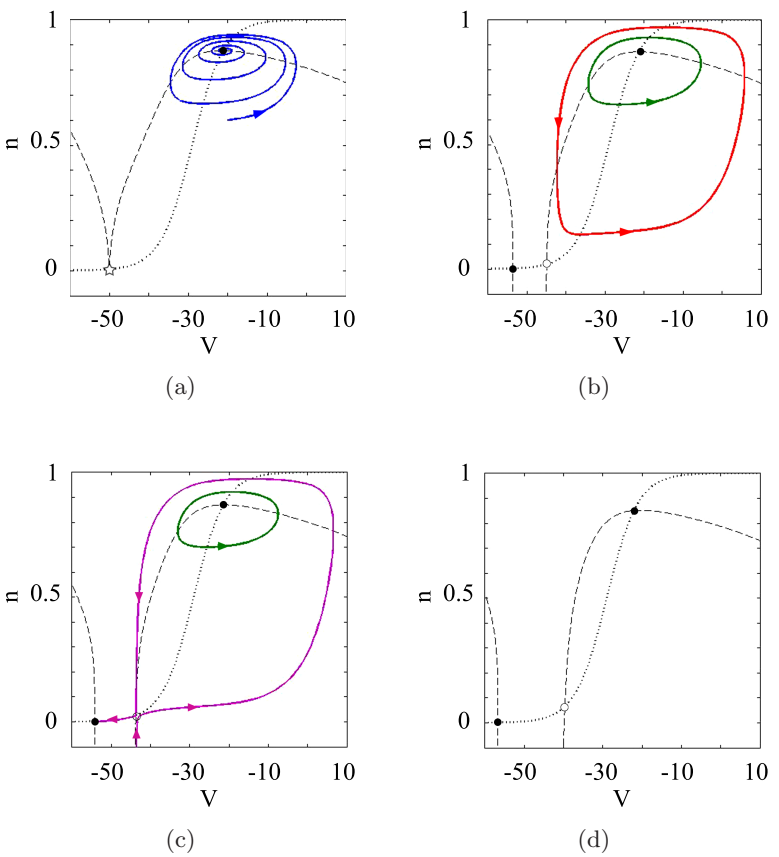

(a) (b) (c) (d)

Fig. 8. Examples of phase portraits on the (V, n)-plane with different values of the slow variable h. (a) $h = 0.468326$, (b) $h = 0.4$, (c) $h = 0.36285$ and (d) $h = 0.124436$. Here the dashed line and dotted line indicate V-nullcline and n-nullcline, respectively. The filled dot, hollow dot and hollow pentagram separately denote stable equilibrium, unstable equilibrium and fold bifurcation point. The red closed curve in phase portrait (b) represents the stable limit cycle; green closed curves in phase portraits (b)–(c) represent the unstable limit cycles; the purple curve in phase portrait (c) represents the homoclinic orbit. Arrows indicate directions of trajectories.

stable node, a saddle and an unstable focus. When $h = 0.36625$, an unstable limit cycle is shrinking, while a stable limit cycle is gradually expanding until it meets the saddle on the middle branch and comes into being as a saddle homoclinic orbit as illustrated in Fig. 6(f).

3.4. "*Fold/Hopf*" *hysteresis loop bursting of point–point type*

Now we discuss the last type of bursting in this neuron model for $g_{\mathrm{K}} = 4.7\,\mathrm{nS}$. The waveform and one-parameter bifurcation diagram are presented in Figs. 7(a) and 7(b), respectively. Although the upper branch of the bifurcation curve in Fig. 7(b) has a Hopf bifurcation and stable and unstable limit cycles, the fast subsystem does not have a limit cycle attractor for any value of the slow variable h. The cause of bursting is that the rate of convergence to the spiking up-state is relatively weak in comparison with the magnitude of $1/\tau_h$. Then the fast variables spend most of their time converging to the equilibrium and the convergence forms damped oscillations. So the system's behavior resembles bursting as illustrated in Fig. 7(a). In Fig. 7(b), with the increase of h, the quiescent down-state corresponding to the stable nodes of the lower branch disappears via fold bifurcation LP_1 at $h = 0.468326$, then transits to the quiescent up-state corresponding to the stable focuses of the upper branch of S-shaped bifurcation curve, but does not transit to the repetitive spiking corresponding to the stable limit cycles. With the decrease of h, the quiescent up-state disappears via a Hopf bifurcation at $h = 0.124436$ and transits to the quiescent down-state. So a point–point type of hysteresis loop is generated by the transitions from one quiescent state to another quiescent state. Therefore, this bursting type exhibits the dynamical properties of "fold/Hopf" hysteresis loop point–point bursting.

In the same manner, we can get several phase portraits on the (V, n)-plane as shown in Fig. 8 if we take some values of h in Fig. 7(b). When $h = 0.468326$, the fast subsystem has two equilibria, which are a saddle-node and a stable focus. With the decrease of h, the fast subsystem has three equilibria and two limit cycles. The large limit cycle is stable and another is unstable. For $h = 0.36285$, the large limit cycle continues to expand and becomes a saddle homoclinic orbit. As $h = 0.124436$, the homoclinic orbit disappears and the unstable limit cycle is reduced to a stable focus.

4. Hopf Bifurcation Analysis

In this section, we will compute the first Lyapunov coefficient of the Hopf bifurcation appearing in the previous section. The Hopf bifurcation is subcritical (supercritical) if the first Lyapunov coefficient is positive (negative). Take the example of the Hopf bifurcation H in Fig. 7(b) ($g_{\mathrm{K}} = 4.7\,\mathrm{nS}$), first, we rewrite the fast subsystems (1) and (2) as

$$\dot{V} = f_1(V, n, h), \tag{11}$$

$$\dot{n} = f_2(V, n, h), \tag{12}$$

where

$$\begin{aligned} f_1 = \frac{1}{C}[&-g_{\mathrm{NaP}} m_{\mathrm{NaP}\infty}(V) h (V - E_{\mathrm{NaP}}) \\ &- g_{\mathrm{Na}} m^3_{\mathrm{Na}\infty}(V)(1 - n)(V - E_{\mathrm{Na}}) \\ &- g_{\mathrm{K}} n^4 (V - E_{\mathrm{K}}) - g_{\mathrm{L}}(V - E_{\mathrm{L}})], \\ f_2 = \frac{\alpha_n(V)(1 - n) - \beta_n(V) n}{\tau_n}, \end{aligned} \tag{13}$$

where $m_{\mathrm{NaP}\infty}(V)$, $m_{\mathrm{Na}\infty}(V)$, $\alpha_n(V)$, $\beta_n(V)$ are defined in Eqs. (4)–(7) and parameters are kept consistent in Table 1.

The Jacobian matrix can be represented as

$$A = \begin{pmatrix} \dfrac{\partial f_1}{\partial V} & \dfrac{\partial f_1}{\partial n} \\ \dfrac{\partial f_2}{\partial V} & \dfrac{\partial f_2}{\partial n} \end{pmatrix},$$

where

$$\begin{aligned} \frac{\partial f_1}{\partial V} = \frac{1}{C}[&-g_{\mathrm{NaP}} \dot{m}_{\mathrm{NaP}\infty}(V) h (V - E_{\mathrm{NaP}}) \\ &- g_{\mathrm{NaP}} m_{\mathrm{NaP}\infty}(V) h - 3 g_{\mathrm{Na}} m^2_{\mathrm{Na}\infty}(V) \\ &\times \dot{m}_{\mathrm{Na}\infty}(V)(1 - n)(V - E_{\mathrm{Na}}) \\ &- g_{\mathrm{Na}} m^3_{\mathrm{Na}\infty}(V)(1 - n) - g_{\mathrm{K}} n^4 - g_{\mathrm{L}}], \\ \frac{\partial f_1}{\partial n} = \frac{1}{C}[&g_{\mathrm{Na}} m^3_{\mathrm{Na}\infty}(V)(V - E_{\mathrm{Na}}) \\ &- 4 g_{\mathrm{K}} n^3 (V - E_{\mathrm{K}})], \\ \frac{\partial f_2}{\partial V} = &\frac{\dot{\alpha}_n(V)(1 - n) - \dot{\beta}_n(V) n}{\tau_n}, \end{aligned}$$

$$\frac{\partial f_2}{\partial n} = \frac{-\alpha_n(V) - \beta_n(V)}{\tau_n},$$
$$\dot{m}_{\mathrm{NaP}\infty}(V) = \frac{e^{-(V+40)/6}}{6[1+e^{-(V+40)/6}]^2},$$
$$\dot{m}_{\mathrm{Na}\infty}(V) = \frac{e^{-(V+34)/5}}{5[1+e^{-(V+34)/5}]^2},$$
$$\dot{\alpha}_n(V) = -\frac{e^{-(V-\theta_n)/(2\sigma_n)}}{2\sigma_n},$$
$$\dot{\beta}_n(V) = \frac{e^{(V-\theta_n)/(2\sigma_n)}}{2\sigma_n}. \tag{14}$$

At the point H in Fig. 7(b), by calculating, we get $h = 0.124436$ and the equilibrium of the fast subsystem (1)–(2) is $(V_0, n_0) = (-22.021386, 0.85127719)$. The corresponding Jacobian matrix is

$$A|_H = \begin{pmatrix} 0.1405224489 & -108.7074129 \\ 0.004447687878 & -0.1405224475 \end{pmatrix},$$

which has a pair of purely imaginary eigenvalues λ, $\overline{\lambda}$, with $\lambda = iw$, $w = 0.680992$. Therefore, there is a Hopf bifurcation in the fast subsystem as shown in Fig. 7(b). Let

$$q = \begin{pmatrix} -0.9793465214 + 0.202087798i \\ 0.00639629796i \end{pmatrix},$$
$$p = \begin{pmatrix} -0.5105445204 \\ 16.13039581 + 78.17021699i \end{pmatrix}$$

satisfy $Aq = iwq$, $A^T p = -iwp$, and $\langle p, q\rangle = 1$. Here $\langle p, q\rangle = \bar{p}_1 q_1 + \bar{p}_2 q_2$ is the standard scalar product in $\mathbb{C}^2$.

In the following, to compute the first Lyapunov coefficient, move the equilibrium of the fast subsystem to the origin of coordinate by making the transformation

$$\begin{cases} V = \xi_1 + V_0, \\ n = \xi_2 + n_0. \end{cases} \tag{15}$$

This transforms system (11)–(12) into

$$\begin{cases} \dot{\xi}_1 = -\dfrac{1}{21}\left\{\dfrac{2.8h(\xi_1+V_0-50)}{1+e^{-(\xi_1+V_0+40)/6}} - \dfrac{28(1-\xi_2-n_0)(\xi_1+V_0-50)}{[1+e^{-(\xi_1+V_0+34)/5}]^3}\right. \\ \qquad\qquad \left. - 4.7(\xi_2+n_0)^4(\xi_1+V_0+85) - 2.8(\xi_1+V_0+57.5)\right\}, \\ \dot{\xi}_2 = \dfrac{1}{20}[e^{(\xi_1+V_0+29)/8}(1-\xi_2-n_0) - e^{-(\xi_1+V_0+29)/8}(\xi_2+n_0)]. \end{cases} \tag{16}$$

This system can be represented as

$$\dot{x} = Ax + F(x), \quad x \in \mathbb{R}^2, \tag{17}$$

where $A = A|_H$, $F(x) = \frac{1}{2}B(x,x) + \frac{1}{6}C(x,x,x) + O(\|x\|^4)$, $B(x,y)$ and $C(x,y,z)$ are symmetric multilinear vector functions which take on the planar vectors $x = (x_1, x_2)^T$, $y = (y_1, y_2)^T$, and $z = (z_1, z_2)^T$. In coordinates, we have

$$B_i(x,y) = \sum_{j,k=1}^{2} \frac{\partial^2 F_i(\xi)}{\partial\xi_j\partial\xi_k}\bigg|_{\xi=0} x_j y_k, \quad i = 1,2, \quad C_i(x,y,z) = \sum_{j,k,l=1}^{2} \frac{\partial^3 F_i(\xi)}{\partial\xi_j\partial\xi_k\partial\xi_l}\bigg|_{\xi=0} x_j y_k z_l, \quad i = 1,2, \tag{18}$$

where $\xi = (\xi_1, \xi_2)^T$.

It is not difficult to calculate

$$B(x,y) = \begin{pmatrix} -0.09027757544x_1y_1 - 3.229500079(x_1y_2 + x_2y_1) \\ -0.01234058236(x_1y_2 + x_2y_1) \end{pmatrix},$$
$$C(x,y,z) = \begin{pmatrix} 0.006323823582x_1y_1z_1 \\ 0.00006949512312x_1y_1z_1 \end{pmatrix}.$$

Then we can simply compute

$$\begin{aligned} g_{20} &= \langle p, B(q,q)\rangle \\ &= 0.05066197946 - 0.03890083991i, \\ g_{11} &= \langle p, B(q,\overline{q})\rangle \\ &= 0.04983675642 + 0.002493882429i, \\ g_{21} &= \langle p, C(q,q,\overline{q})\rangle \\ &= 0.003161782429 + 0.004894127457i \end{aligned}$$

and calculate the first Lyapunov coefficient at H by formula (3.20) in [Kuznetsov, 1998],

$$\begin{aligned} l_1(0) &= \frac{1}{2w^2}\mathrm{Re}(ig_{20}g_{11} + wg_{21}) \\ &= 0.0042754657 > 0. \end{aligned}$$

Hence the Hopf bifurcation point H in Fig. 7(b) is subcritical.

5. Codimension-Two Bifurcation Analysis of the Whole System

5.1. *Bifurcations in the (V_e, g_{K})-plane*

In this section, we exhibit the bifurcation analysis of the whole system (1)–(3) by numerical simulation with fixed parameter values denoted in Table 1. Figure 9(a) is a global structure of the two-parameter bifurcation diagram in the (V_e, g_{K})-plane. Figures 9(b)–9(d) are the enlarged bifurcation diagrams of Fig. 9(a). In Figs. 9(a)–9(d), h_1 and h_2 indicate the Hopf bifurcation curves; f_1 and f_2 denote the fold bifurcation curves; CP_i $(i = 1, 2)$ represents the cusp bifurcation; BT represents the Bogdanov–Takens bifurcation; GH_i $(i = 1, 2, 3, 4, 5, 6)$ represents the generalized Hopf (or Bautin) bifurcation; NS represents the zero Neutral Saddle bifurcation. For the meaning of these bifurcations, the reader is referred to [Guckenheimer & Holmes, 1983; Kuznetsov, 1998]. Some data related to these bifurcation points are listed in Table 2.

In Fig. 9(a), we can see that the Hopf bifurcation curve h_1 (straight line) is independent of the parameter g_{K}. And there is no codimension-two bifurcation point on this curve. Then we look at the other three bifurcation curves. The branches of f_1 and f_2 terminate at the cusp point CP_2 (45.752884, −2.597061) where the eigenvalues are $\lambda_1 = 0$, $\lambda_2 = -0.00592119$, $\lambda_3 = 0.280925$. The fold bifurcation curve f_2 is divided into two sections by the cusp point CP_1 (39.336876, −2.155251) where the eigenvalues are $\lambda_1 = 0$, $\lambda_2 = -0.434235$, $\lambda_3 = 0.00038313$.

Near the point CP_i $(i = 1, 2)$, system (1)–(3) is equivalent to the following topological normal form

$$\begin{cases} \dot{\xi} = \beta_1 + \beta_2\xi + \sigma\xi^3, \\ \dot{\eta}_- = -\eta_-, \\ \dot{\eta}_+ = \eta_+, \end{cases} \tag{19}$$

where

$$\eta_\pm \in \mathbb{R}^1, \quad \beta_{1,2} \in \mathbb{R},$$

$$\sigma = \mathrm{sign}(c) = \begin{cases} 1, & \text{for } \mathrm{CP}_1, \\ -1, & \text{for } \mathrm{CP}_2. \end{cases}$$

A Bogdanov–Takens bifurcation takes place at the point labeled BT (39.519172, −2.15726) with two zero eigenvalues $\lambda_{1,2} = 0$ and one nonzero real eigenvalue $\lambda_3 = -0.4908234728$. The point BT is the tangency point of the Hopf bifurcation curve h_2 and the fold bifurcation curve f_2. Near the point BT, system (1)–(3) can be reduced to the following topological normal form

$$\begin{cases} \dot{\eta}_1 = \eta_2, \\ \dot{\eta}_2 = \beta_1 + \beta_2\eta_1 + \eta_1^2 + s\eta_1\eta_2, \end{cases} \tag{20}$$

where $a = -9.080841 \times 10^{-7}$, $b = -2.037929 \times 10^{-3}$, $s = \mathrm{sign}(ab) = 1$.

There are six generalized Hopf bifurcations in the Hopf bifurcation curve h_2. At the point GH_i $(i = 1, 2, 3, 4, 5, 6)$, the system (1)–(3) has one real eigenvalue and a pair of purely imaginary eigenvalues. Furthermore, the first Lyapunov coefficient is equal to 0. Near the point GH_i $(i = 1, 2, 3, 4, 5, 6)$, system (1)–(3) is locally topologically equivalent to the following complex normal form

$$\begin{cases} \dot{z} = (\beta_1 + i)z + \beta_2 z|z|^2 + sz|z|^4, \quad z \in \mathbb{C}^1, \\ \dot{\eta}_- = -\eta_-, \quad \eta_- \in \mathbb{R}^1, \end{cases} \tag{21}$$

where l_2 is the second Lyapunov coefficient and

$$s = \mathrm{sign}(l_2) = \begin{cases} 1, & \text{for } \mathrm{GH}_i \ (i = 3, 5, 6), \\ -1, & \text{for } \mathrm{GH}_j \ (j = 1, 2, 4). \end{cases}$$

There exists a zero Neutral Saddle bifurcation in the fold bifurcation curve f_2 labeled NS (45.203946, −2.48432) with one zero eigenvalue $\lambda_1 = 0$ and two real eigenvalues satisfying $\lambda_2 + \lambda_3 = 0$.

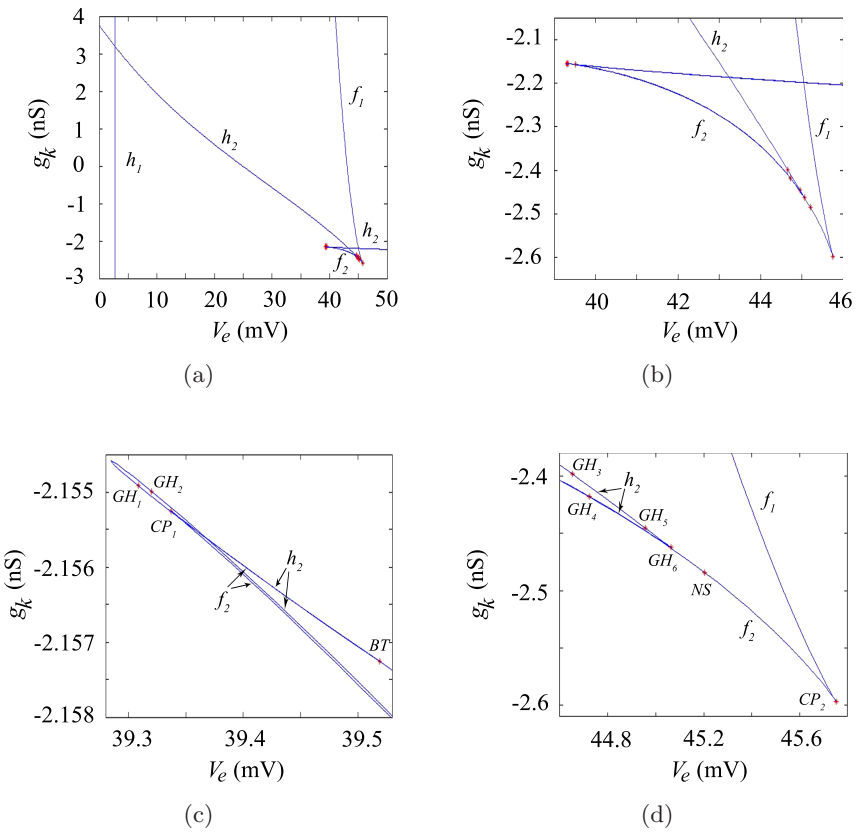

Fig. 9. Codimension-two bifurcation analysis of the whole system. (a) Representation of the two-parameter bifurcation diagram in the (V_e, g_K)-plane. (b)–(d) The enlarged bifurcation diagrams of (a). The labels represent the following bifurcations: CP — cusp, BT — Bogdanov–Takens, GH — generalized Hopf (or Bautin), NS — zero neutral saddle. Besides, h_1 and h_2 are the Hopf bifurcation curves, and f_1 and f_2 are the fold bifurcation curves.

Table 2. Data related to the special points.

Points	Parameter Values (V_e, g_K)	Eigenvalues λ_1, λ_2, λ_3	Normal Form Parameter
CP_1	(39.336876, −2.155251)	$\lambda_1 = 0$, $\lambda_2 = -0.434235$, $\lambda_3 = 0.00038313$	$c = 6.355374 \times 10^{-4}$
CP_2	(45.752884, −2.597061)	$\lambda_1 = 0$, $\lambda_2 = -0.00592119$, $\lambda_3 = 0.280925$	$c = -1.763739 \times 10^{-4}$
BT	(39.519172, −2.15726)	$\lambda_{1,2} = 0$, $\lambda_3 = -0.4908234728$	$a = -9.080841 \times 10^{-7}$, $b = -2.037929 \times 10^{-3}$
GH_1	(39.308659, −2.154919)	$\lambda_1 = -0.44761$, $\lambda_{2,3} = \pm 0.000520476i$	$l_2 = -1.172727 \times 10^{-3}$
GH_2	(39.320244, −2.154993)	$\lambda_1 = -0.405652$, $\lambda_{2,3} = \pm 0.000736812i$	$l_2 = -5.713233 \times 10^{-4}$
GH_3	(44.651508, −2.39805)	$\lambda_1 = -0.000472917$, $\lambda_{2,3} = \pm 0.071716i$	$l_2 = 2.243264 \times 10^{-3}$
GH_4	(44.722346, −2.417798)	$\lambda_1 = -0.0649106$, $\lambda_{2,3} = \pm 0.00267965i$	$l_2 = -3.273501$
GH_5	(44.955248, −2.445208)	$\lambda_1 = -0.000676546$, $\lambda_{2,3} = \pm 0.0400693i$	$l_2 = 0.294592$
GH_6	(45.063059, −2.462362)	$\lambda_1 = -0.00508465$, $\lambda_{2,3} = \pm 0.0100635i$	$l_2 = 692.4995$
NS	(45.203946, −2.48432)	$\lambda_1 = 0$, $\lambda_{2,3} = \pm 0.0355362$	*None*

5.2. *Bogdanov–Takens bifurcation analysis*

In this section, we research the Bogdanov–Takens bifurcation of the whole system (1)–(3) by the method proposed by Carrillo *et al.* [2010]. In Fig. 9(c), the Bogdanov–Takens bifurcation point BT appears when

$$(V_e, g_{\mathrm{K}}) = (39.519172, -2.15726) \triangleq \mu_0.$$

Now the equilibrium of the whole system (1)–(3) is $(V, n, h) = (-11.721, 0.98687, 0.0023605) \triangleq X_0$.

First, we rewrite the whole system (1)–(3) as

$$\frac{dX}{dt} = F(X, \mu) = \begin{pmatrix} f_1(X, \mu) \\ f_2(X, \mu) \\ f_3(X, \mu) \end{pmatrix}, \tag{22}$$

where $X = (V, n, h)^T$, $\mu = (V_e, g_{\mathrm{K}})^T$, and

$$\begin{aligned} f_1(X, \mu) = \frac{1}{C}[&-g_{\mathrm{NaP}} m_{\mathrm{NaP}\infty}(V) h (V + V_e - E_{\mathrm{NaP}}) \\ &- g_{\mathrm{Na}} m^3_{\mathrm{Na}\infty}(V)(1 - n)(V + V_e - E_{\mathrm{Na}}) \\ &- g_{\mathrm{K}} n^4 (V + V_e - E_{\mathrm{K}}) \\ &- g_{\mathrm{L}}(V + V_e - E_{\mathrm{L}})], \\ f_2(X, \mu) = \frac{\alpha_n(V)(1 - n) - \beta_n(V) n}{\tau_n}&, \\ f_3(X, \mu) = \frac{\alpha_h(V)(1 - h) - \beta_h(V) h}{\tau_h}&, \end{aligned} \tag{23}$$

where $m_{\mathrm{NaP}\infty}(V)$, $m_{\mathrm{Na}\infty}(V)$, $\alpha_n(V)$, $\alpha_h(V)$, $\beta_n(V)$, $\beta_h(V)$ are defined in Eqs. (4)–(7) and parameters are kept consistent in Table 1.

Let us consider the Taylor series of $F(X, \mu)$ around (X_0, μ_0),

$$\begin{aligned} F(X, \mu) = &DF(X_0, \mu_0)(X - X_0) \\ &+ F_\mu(X_0, \mu_0)(\mu - \mu_0) \\ &+ \frac{1}{2} D^2 F(X_0, \mu_0)(X - X_0, X - X_0) \\ &+ F_{\mu X}(X_0, \mu_0)(\mu - \mu_0, X - X_0) + \cdots. \end{aligned} \tag{24}$$

Note

$$A_1 \triangleq DF(X_0, \mu_0) = \left.\begin{pmatrix} \dfrac{\partial f_1}{\partial V} & \dfrac{\partial f_1}{\partial n} & \dfrac{\partial f_1}{\partial h} \\ \dfrac{\partial f_2}{\partial V} & \dfrac{\partial f_2}{\partial n} & \dfrac{\partial f_2}{\partial h} \\ \dfrac{\partial f_3}{\partial V} & \dfrac{\partial f_3}{\partial n} & \dfrac{\partial f_3}{\partial h} \end{pmatrix}\right|_{(X_0, \mu_0)}$$

$$= \begin{pmatrix} -0.05052336025 & 15.95289677 & 2.93390807 \\ 0.001422893352 & -0.4392696686 & 0 \\ -4.043966734 \times 10^{-7} & 0 & -0.00103033198 \end{pmatrix},$$

$$F_\mu(X_0, \mu_0) = \left.\begin{pmatrix} \dfrac{\partial f_1}{\partial V_e} & \dfrac{\partial f_1}{\partial g_{\mathrm{K}}} \\ \dfrac{\partial f_2}{\partial V_e} & \dfrac{\partial f_2}{\partial g_{\mathrm{K}}} \\ \dfrac{\partial f_3}{\partial V_e} & \dfrac{\partial f_3}{\partial g_{\mathrm{K}}} \end{pmatrix}\right|_{(X_0, \mu_0)} = \begin{pmatrix} -0.05311922025 & -5.09474621 \\ 0 & 0 \\ 0 & 0 \end{pmatrix}.$$

The matrix A_1 has three eigenvalues, namely, 0, 0, and -0.4908234728. Let $P = (p_1, p_2, P_0)$ be an invertible matrix, which satisfies $P^{-1} A_1 P = J$, where $J = \begin{pmatrix} J_0 & 0 \\ 0 & J_1 \end{pmatrix}$, $J_0 = \begin{pmatrix} 0 & 1 \\ 0 & 0 \end{pmatrix}$, $J_1 = -0.4908234728$, p_1, p_2 are generalized eigenvectors of the matrix A_1 corresponding to the double-zero

eigenvalue and P_0 contains the generalized eigenvectors of the matrix J_1. Then we obtain

$$p_1 = (1, 0.003238830447, -0.0003924437902)^T,$$
$$p_2 = (1, -0.004133991543, 0.3804981318)^T,$$
$$P_0 = (-36.23159257, 1, -0.00002991454481)^T.$$

If we define $P^{-1} = (q_1, q_2, Q_0^T)^T$, then

$$q_1 = (0.8942746637, 32.40093551, -1.998247578)^T,$$
$$q_2 = (0.0009221228139, 0.03348853589, 2.626074177)^T,$$
$$Q_0 = (-0.002892591961, 0.895197305, 0.01732815354).$$

By calculating expressions (28) and (29) in [Carrillo *et al.*, 2010], then we get

$$\begin{aligned}
a &= \frac{1}{2} p_1^T (q_2 \cdot D^2 F(X_0, \mu_0)) p_1 \\
&= -9.078787855 \times 10^{-7}, \\
b &= p_1^T (q_1 \cdot D^2 F(X_0, \mu_0)) p_1 \\
&\quad + p_1^T (q_2 \cdot D^2 F(X_0, \mu_0)) p_2 \\
&= -0.002037531361, \\
S_1 &= F_\mu^T (X_0, \mu_0) q_2 \\
&= (-0.00004898244485, -0.004697981711)^T, \\
S_2 &= \left[\frac{2a}{b} (p_1^T (q_1 \cdot D^2 F(X_0, \mu_0)) p_2 \right. \\
&\quad + p_2^T (q_2 \cdot D^2 F(X_0, \mu_0)) p_2) \\
&\quad \left. - p_1^T (q_2 \cdot D^2 F(X_0, \mu_0)) p_2 \right] F_\mu^T (X_0, \mu_0) q_1 \\
&\quad - \frac{2a}{b} \sum_{i=1}^{2} (q_i \cdot (F_{\mu X}(X_0, \mu_0) - ((P_0 J_1^{-1} Q_0) \\
&\quad \times F_\mu(X_0, \mu_0))^T \times D^2 F(X_0, \mu_0))) p_i \\
&\quad + (q_2 \cdot (F_{\mu X}(X_0, \mu_0) - ((P_0 J_1^{-1} Q_0) \\
&\quad \times F_\mu(X_0, \mu_0))^T \times D^2 F(X_0, \mu_0))) p_1 \\
&= (-5.504274272, 0.3645960161)^T.
\end{aligned}$$

If we choose $\overline{\lambda}_1$, $\overline{\lambda}_2$ as bifurcation parameters, where $\overline{\lambda}_1 = V_e - 39.519172$, $\overline{\lambda}_2 = g_{\mathrm{K}} + 2.15726$, then

$$\begin{aligned}
\beta_1 &= S_1^T (\mu - \mu_0) \\
&= -0.00004898244485 \overline{\lambda}_1 - 0.004697981711 \overline{\lambda}_2, \\
\beta_2 &= S_2^T (\mu - \mu_0) \\
&= -5.504274272 \overline{\lambda}_1 + 0.3645960161 \overline{\lambda}_2.
\end{aligned}$$

Using Theorem 1 in [Carrillo *et al.*, 2010], the whole system (1)–(3) at $X = X_0$, $\mu \approx \mu_0$, is locally topologically equivalent to

$$\begin{cases}
\dfrac{dz_1}{dt} = z_2, \\
\dfrac{dz_2}{dt} = \beta_1 + \beta_2 z_1 + a z_1^2 + b z_1 z_2 \\
\qquad = -0.00004898244485 \overline{\lambda}_1 - 0.004697981711 \overline{\lambda}_2 \\
\qquad\quad + (-5.504274272 \overline{\lambda}_1 + 0.3645960161 \overline{\lambda}_2) z_1 \\
\qquad\quad - 9.078787855 \times 10^{-7} z_1^2 \\
\qquad\quad - 0.002037531361 z_1 z_2.
\end{cases} \tag{25}$$

Making the transformation of variables by

$$t = \left| \frac{b}{a} \right| t_1 = \frac{0.002037531361}{9.078787855 \times 10^{-7}} t_1,$$
$$z_1 = \frac{a}{b^2} \eta_1 = \frac{-9.078787855 \times 10^{-7}}{(-0.002037531361)^2} \eta_1,$$
$$z_2 = \operatorname{sign}\left(\frac{b}{a} \right) \frac{a^2}{b^3} \eta_2 = \frac{(-9.078787855 \times 10^{-7})^2}{(-0.002037531361)^3} \eta_2,$$

system (25) becomes

$$\begin{cases}
\dfrac{d\eta_1}{dt_1} = \eta_2, \\
\dfrac{d\eta_2}{dt_1} = \overline{\beta}_1 + \overline{\beta}_2 \eta_1 + \eta_1^2 + s \eta_1 \eta_2,
\end{cases} \tag{26}$$

where

$$\begin{aligned}
\overline{\beta}_1 &= \frac{b^4}{a^3} \beta_1 \\
&= 1.12816874 \times 10^3 \overline{\lambda}_1 + 1.082044011 \times 10^5 \overline{\lambda}_2, \\
\overline{\beta}_2 &= \frac{b^2}{a^2} \beta_2 \\
&= -2.772381129 \times 10^7 \overline{\lambda}_1 + 1.83638944 \times 10^6 \overline{\lambda}_2, \\
s &= \operatorname{sign}(ab) = 1.
\end{aligned}$$

Since

$$\begin{aligned}
4\overline{\beta}_1 - \overline{\beta}_2^2 = 0 \Leftrightarrow\ & 1.703224183 \times 10^{11}\overline{\lambda}_1^2 \\
& - 2.256387386 \times 10^{10}\overline{\lambda}_1\overline{\lambda}_2 \\
& + 7.473009256 \times 10^{8}\overline{\lambda}_2^2 - \overline{\lambda}_1 \\
& - 95.91153988\overline{\lambda}_2 = 0, \\
\overline{\beta}_1 = 0 \Leftrightarrow\ & \overline{\lambda}_1 = -95.91153988\overline{\lambda}_2, \\
\overline{\beta}_2 < 0 \Leftrightarrow\ & \overline{\lambda}_2 < 15.09691283\overline{\lambda}_1, \\
\overline{\beta}_1 + \frac{6}{25}\overline{\beta}_2^2 = o(\overline{\beta}_2^2) \Leftrightarrow\ & 1.635095216 \times 10^{11}\overline{\lambda}_1^2 \\
& - 2.166131891 \times 10^{10}\overline{\lambda}_1\overline{\lambda}_2 \\
& + 7.174088887 \times 10^{8}\overline{\lambda}_2^2 + \overline{\lambda}_1 \\
& + 95.91153988\overline{\lambda}_2 \\
= & \ o(|\overline{\lambda}_1, \overline{\lambda}_2|^2).
\end{aligned}$$

According to the theory on Bogdanov–Takens bifurcation in [Kuznetsov, 1998] and the preceding analysis, we have

Theorem 1. *Let* $\overline{\lambda}_1 = V_e - 39.519172$ *and* $\overline{\lambda}_2 = g_{\mathrm{K}} + 2.15726$. *Then system (1)–(3) is locally topologically equivalent to the following system at the Bogdanov–Takens bifurcation point BT if bifurcation parameters* (V_e, g_{K}) *vary around* $(39.519172, -2.15726)$:

$$\begin{cases}
\dfrac{d\eta_1}{dt_1} = \eta_2, \\
\dfrac{d\eta_2}{dt_1} = 1.12816874 \times 10^{3}\overline{\lambda}_1 \\
\qquad + 1.082044011 \times 10^{5}\overline{\lambda}_2 \\
\qquad + (-2.772381129 \times 10^{7}\overline{\lambda}_1 \\
\qquad + 1.83638944 \times 10^{6}\overline{\lambda}_2)\eta_1 + \eta_1^2 + \eta_1\eta_2.
\end{cases} \tag{27}$$

System (27) has three bifurcation curves in a small neighborhood of the origin:

(1) *the local representation of a fold bifurcation curve is*

$$\begin{aligned}
T = \{(\overline{\lambda}_1, \overline{\lambda}_2) : & 1.703224183 \times 10^{11}\overline{\lambda}_1^2 \\
& - 2.256387386 \times 10^{10}\overline{\lambda}_1\overline{\lambda}_2 \\
& + 7.473009256 \times 10^{8}\overline{\lambda}_2^2 - \overline{\lambda}_1 \\
& - 95.91153988\overline{\lambda}_2 = 0\};
\end{aligned}$$

(2) *the local representation of a nondegenerate Hopf bifurcation curve is*

$$H = \{(\overline{\lambda}_1, \overline{\lambda}_2) : \overline{\lambda}_1 = -95.91153988\overline{\lambda}_2, \overline{\lambda}_2 < 0\};$$

(3) *the local representation of a saddle homoclinic bifurcation curve is*

$$\begin{aligned}
P = \{(\overline{\lambda}_1, \overline{\lambda}_2) : & 1.635095216 \times 10^{11}\overline{\lambda}_1^2 \\
& - 2.166131891 \times 10^{10}\overline{\lambda}_1\overline{\lambda}_2 \\
& + 7.174088887 \times 10^{8}\overline{\lambda}_2^2 + \overline{\lambda}_1 \\
& + 95.91153988\overline{\lambda}_2 = o(|\overline{\lambda}_1, \overline{\lambda}_2|^2), \\
& \overline{\lambda}_2 < 15.09691283\overline{\lambda}_1\}.
\end{aligned}$$

6. Conclusions

Respiratory movement in mammals is a kind of neural activity, which is produced by the neural network composed of neurons in the lower brain. Therefore, it is of great significance to research the discharge characteristics of these neurons for understanding the transmission of nerve electrical signal in neural networks. As a manner of neural information coding, bursting and spiking can well depict the properties of neural electrical activity. In this article, we have investigated the mechanisms underlying bursting and spiking and analyzed their dynamics. Based on the pre-Bötzinger complex respiratory neuron model, fast–slow dynamics analysis and phase plane analysis are performed from the perspective of bursting classification. In particular, we find four types of fast–slow bursters by modulating the parameter g_{K}. These four types of bursting are "circle/homoclinic" bursting via the "circle/homoclinic" hysteresis loop, "fold/homoclinic" bursting via the "fold/homoclinic" hysteresis loop, "fold circle/homoclinic" bursting via the "fold/homoclinic" hysteresis loop, and "fold/Hopf" hysteresis loop bursting of point–point type. With the decreasing of parameter g_{K}, firing patterns of this model vary from tonic spiking to bursting. In addition, the sign of the first Lyapunov coefficient at Hopf bifurcation point is computed to decide whether it is supercritical or subcritical or not. When the first Lyapunov coefficient is positive, the Hopf bifurcation is subcritical. For two-parameter bifurcation analysis, we mainly discuss the Bogdanov–Takens bifurcation point. We not only calculate the topological normal form of the whole system to the center manifold, but also give three bifurcation curves, which are a fold

bifurcation curve, a nondegenerate Hopf bifurcation curve, and a saddle homoclinic bifurcation curve. When the fold bifurcation curve is very close to the Hopf bifurcation curve, it is quite difficult to draw the homoclinic bifurcation curve by software such as MATCONT [Dhooge *et al.*, 2003; Dhooge *et al.*, 2006]. But we can theoretically determine the equation of this curve by the method described above. Our obtained results may provide an instruction for a further investigation of other neuronal cells.

Acknowledgment

This work was supported by the National Natural Science Foundation of China under Grant Nos. 11572127 and 11172103.

References

Bacak, B. J., Segaran, J. & Molkov, Y. I. [2016] "Modeling the effects of extracellular potassium on bursting properties in pre-Bötzinger complex neurons," *J. Comput. Neurosci.* **40**, 231–245.

Butera, R. J., Rinzel, J. R. & Smith, J. C. [1999] "Models of respiratory rhythm generation in the pre-Bötzinger complex. I: Bursting pacemaker neurons," *J. Neurophysiol.* **82**, 382–397.

Carrillo, F. A., Verduzco, F. & Delgado, J. [2010] "Analysis of the Takens–Bogdanov bifurcation on m-parameterized vector fields," *Int. J. Bifurcation and Chaos* **20**, 995–1005.

Che, Y., Wang, J., Deng, B., Wei, X. & Han, C. [2012] "Bifurcations in the Hodgkin–Huxley model exposed to DC electric fields," *Neurocomputing* **81**, 41–48.

Che, Y., Li, H., Han, C., Wei, X., Deng, B. & Wang, J. [2014] "Effects of DC electric fields on neuronal excitability: A bifurcation analysis," *Int. J. Mod. Phys. B* **28**, 5447–5452.

Dhooge, A., Govaerts, W. & Kuznetsov, Y. A. [2003] "MATCONT: A MATLAB package for numerical bifurcation analysis of ODEs," *ACM Trans. Math. Softw.* **29**, 141–164.

Dhooge, A., Govaerts, W., Kuznetsov, Y. A., Mestrom, W., Riet, A. M. & Sautois, B. [2006] *MATCONT and CL MATCONT: Continuation Toolboxes in MATLAB* (Utrecht University, The Netherlands).

Eyherabide, H. G., Rokem, A., Herz, A. V. & Samengo, I. [2009] "Bursts generate a non-reducible spike-pattern code," *Front Neurosci.* **3**, 8–14.

Feldman, J. L. & Smith, J. C. [1989] "Cellular mechanisms underlying modulation of breathing pattern in mammals," *Ann. NY Acad. Sci.* **563**, 114–130.

Fenichel, N. [1979] "Geometric singular perturbation theory for ordinary differential equations," *J. Diff. Eqs.* **31**, 53–98.

Guckenheimer, J. & Holmes, P. [1983] *Nonlinear Oscillations, Dynamical Systems and Bifurcations of Vector Fields* (Springer-Verlag, NY).

Hoppensteadt, F. C. [1993] *Analysis and Simulations of Chaotic Systems* (Springer-Verlag, NY).

Huerta, P. T. & Lisman, J. E. [1995] "Bidirectional synaptic plasticity induced by a single burst during cholinergic theta oscillation in CA1 *in vitro*," *Neuron* **15**, 1053–1063.

Izhikevich, E. M. [2000] "Neural excitability, spiking and bursting," *Int. J. Bifurcation and Chaos* **10**, 1171–1266.

Izhikevich, E. M. [2003] "Bursts as a unit of neural information: Selective communication via resonance," *Trends Neurosci.* **26**, 161–167.

Izhikevich, E. M. & Hippensteadt, F. [2004] "Classification of bursting mappings," *Int. J. Bifurcation and Chaos* **14**, 3847–3854.

Izhikevich, E. M. [2005] *Dynamical Systems in Neuroscience: The Geometry of Excitability and Bursting* (MIT Press).

Johnson, S. M., Smith, J. C., Funk, G. D. & Feldman, J. L. [1994] "Pacemaker behavior of respiratory neurons in medullary slices from neonatal rat," *J. Neurophysiol.* **72**, 2598–2608.

Jones, C. K. R. T. [1995] "Geometric singular perturbation theory," *Dynamical Systems*, Lecture Notes in Mathematics, Vol. 1609 (Springer, Berlin, Heidelberg), pp. 44–118.

Koshiya, N. & Smith, J. C. [1999] "Neuronal pacemaker for breathing visualized *in vitro*," *Nature* **400**, 360–363.

Kotnik, T., Pucihar, G. & Miklavčič, D. [2011] *Clinical Aspects of Electroporation* (Springer).

Kuznetsov, Y. A. [1998] *Elements of Applied Bifurcation Theory* (Springer-Verlag, NY).

Lisman, J. E. [1997] "Bursts as a unit of neural information: Making unreliable synapses reliable," *Trends Neurosci.* **20**, 38–73.

Lu, B., Liu, S., Liu, X., Jiang, X. & Wang, X. [2016] "Bifurcation and spike adding transition in Chay–Keizer model," *Int. J. Bifurcation and Chaos* **26**, 1650090-1–13.

Mishchenko, E. F., Kolesov, Y. S., Kolesov, A. Y. & Rozov, N. K. [1994] *Asymptotic Methods in Singularly Perturbed Systems* (Plenum Press, NY).

Negro, C. A. D., Johnson, S. M., Butera, R. J. & Smith, J. C. [2001] "Models of respiratory rhythm generation in the pre-Bötzinger complex. III: Experimental tests of model predictions," *J. Neurophysiol.* **86**, 59–74.

Polk, C. & Postow, E. [1996] *Handbook of Biological Effects of Electromagnetic Fields* (CRC Press, Boca Raton).

Rekling, J. C. & Feldman, J. L. [1998] "Pre-Bötzinger complex and pacemaker neurons: Hypothesized site

and kernel for respiratory rhythm generation," *Ann. Rev. Physiol.* **60**, 385–405.

Rybak, I. A., Shevtsova, N. A., St-John, W. M., Paton, J. F. R. & Pierrefiche, O. [2003] "Endogenous rhythm generation in the pre-Bötzinger complex and ionic currents: Modelling and *in vitro* studies," *Eur. J. Neurosci.* **18**, 239–257.

Rybak, I. A., Shevtsova, N. A., Ptak, K. & Mccrimmon, D. R. [2004] "Intrinsic bursting activity in the pre-Bötzinger complex: Role of persistent sodium and potassium currents," *Biol. Cybern.* **90**, 59–74.

Shao, X. M. & Feldman, J. L. [1997] "Respiratory rhythm generation and synaptic inhibition of expiratory neurons in pre-Bötzinger complex: Differential roles of glycinergic and GABAergic neural transmission," *J. Neurophysiol.* **77**, 1853–1860.

Shevtsova, N. A., Ptak, K., Mccrimmon, D. R. & Rybak, I. A. [2003] "Computational modeling of bursting pacemaker neurons in the pre-Bötzinger complex," *Neurocomputing* **52–54**, 933–942.

Smith, D. R. [1985] *Singular-Perturbation Theory, An Introduction with Applications* (Cambridge University Press, Cambridge).

Smith, J. C., Ellenberger, H. H., Ballanyi, K., Richter, D. & Feldman, J. L. [1991] "Pre-Bötzinger complex: A brainstem region that may generate respiratory rhythm in mammals," *Science* **254**, 726–729.

Smith, J. C., Abdala, A. P., Borgmann, A., Rybak, I. A. & Paton, J. F. [2013] "Brainstem respiratory networks: Building blocks and microcircuits," *Trends Neurosci.* **36**, 152–162.

Thoby-Brisson, M. & Ramirez, J. M. [2001] "Identification of two types of inspiratory pacemaker neurons in the isolated respiratory network of mice," *J. Neurophysiol.* **86**, 104–112.

Wang, X. J. [1999] "Fast burst firing and short-term synaptic plasticity: A model of neocortical chattering neurons," *Neuroscience* **89**, 347–362.

Wang, H., Lu, Q. & Wang, Q. [2008] "Bursting and synchronization transition in the coupled modified ML neurons," *Commun. Nonlin. Sci. Numer. Simulat.* **13**, 1668–1675.

Wang, J., Liu, S., Liu, X. & Zeng, Y. [2015] "Bifurcation and firing patterns of the pancreatic β-cell," *Int. J. Bifurcation and Chaos* **25**, 1530024-1–11.

Yang, Z. & Lu, Q. [2007] "Transitions from bursting to spiking due to depolarizing current in the Chay neuronal model," *Commun. Nonlin. Sci. Numer. Simulat.* **12**, 357–365.